Role of the pedestal position on the pedestal performance in AUG, JET-ILW and TCV and implications for ITER

(Article begins on next page)

23 June 2024

ROLE OF THE PEDESTAL POSITION ON THE PEDESTAL PERFORMANCE IN AUG, JET-ILW AND TCV AND IMPLICATIONS FOR ITER

L.Frassinetti[1], M.G. Dunne[2], U. Sheikh[3], S. Saarelma[4], C. M. Roach[4], E.Stefanikova[1], C. Maggi[4], L. Horvath[5], S. Pamela[4], E. de la Luna[6], E. Wolfrum[2], M. Bernert[2], P. Blanchard[3], B. Labit[3], A. Merle[3], L. Guimarais[7], S. Coda[3], H. Meyer[4], J.C. Hillesheim[4], the ASDEX Upgrade Team[2], JET contributors[8*], the TCV team[3**] and the EUROfusion MST1 Team[***]

EUROfusion Consortium, JET, Culham Science Centre, Abingdon, OX14 3DB, UK
[1]Division of Fusion Plasma Physics, KTH, Stockholm SE
[2]Max-Planck-Institut für Plasmaphysik, Garching, Germany
[3] Swiss Plasma Center (SPC), Ecole Polytechnique Fédérale de Lausanne (EPFL), Lausanne,Switzerland
[4]CCFE, Culham Science Centre, Abingdon, OX14 3DB, UK
[5]York Plasma Institute, University of York, York, YO10 5DD, UK
[6]Laboratorio Nacional de Fusion CIEMAT, Madrid, Spain
[7]Instituto de Plasmas e Fusão Nuclear, Universidade de Lisboa
[8]EUROfusion Consortium, JET, Culham Science Centre, Abingdon, OX14 3DB, UK
* see X. Litaudon et al., Nuclear Fusion 57, 102001 (2017)
**see Coda et al., Nuclear Fusion 57, 102011 (2017)
*** see H. Meyer et al., Nuclear Fusion 57, 102014 (2017)

Abstract

The role of the pedestal position on the pedestal performance has been investigated in AUG, JET-ILW and TCV. When the pedestal is peeling-ballooning (PB) limited, the three machines show a similar behaviour. The outward shift of the pedestal density relative to the pedestal temperature can lead to the outward shift of the pedestal pressure which, in turns, reduces the PB stability, degrades the pedestal confinement and reduces the pedestal width. Once the experimental density position is considered, the EPED model is able to correctly predict the pedestal height. An estimate of the impact of the density position on a ITER baseline scenario shows that the maximum reduction in the pedestal height is 10% while the reduction in the fusion power is between 10% and 40% depending on the assumptions for the core transport model used.

In other plasmas, where the pedestal density is shifted even more outwards relative to the pedestal temperature, the pedestal does not seem PB limited and a different behaviour is observed. The outward shift of the density is still empirically correlated with the pedestal degradation but no change in the pressure position is observed and the PB model is not able to correctly predict the pedestal height. On the other hand, the outward shift of the density leads to a significant increase of η_e and η_e (where $\eta_{e,i}$ is the ratio of density to temperature scale lengths, $\eta_{e,i} = L_{ne,i}/L_{Te,i}$) which leads to the increase of the growth rate of microinstabilities (mainly ETG and ITG) by 50%. This suggests that, in these plasmas, the increase in the turbulent transport due to the outward shift of the density might play an important role in the decrease of the pedestal performance.

1. INTRODUCTION

Differences in the pedestal position of electron density (n_e^{pos}) and temperature (T_e^{pos}) have been experimentally known for several years. The first evidence was shown in 1996 [1] during dimensionless scan experiments in JET, where an outward shift of the pedestal density was correlated with the increased fuelling rate. In this early work, no detailed investigation was possible due to the lack of appropriate diagnostics but, still, the authors speculated that the change in n_e^{pos} could have been, somehow, at the orgin of the confinement degradation with increasing fuelling rate. In more recent years, a small difference in n_e^{pos} and T_e^{pos} has been observed in DIII-D and in the carbon wall JET (JET-C) [2, 3]. While the difference was relatively small (lower than 0.5cm on the midplane) and while no significant impact on the MHD stability was estimated for DIII-D, it was pointed out that future predictive pedestal models might have needed to take into account the position of the pedestal density. In the same period, experiments in NSTX have shown that the confinement improvement due to lithium-wall coating was related to the low-*n* peeling or ballooning modes stabilization produced by an inward shift of the pedestal density [4,5]. The lithium seeding led to a confinement improvement (via an inward shift of n_e^{pos}) also in DIII-D [6]. Density shifts have been observed also in Alcator C-mod [7].

The systematic study of the role of the pedestal position in the peeling-ballooning (PB) modes stability and in the pedestal performance has started since 2016 in ASDEX Upgrade (AUG) [8], JET [9,10] and TCV [11]. Interestingly, so far the AUG and TCV results have been in apparent contradiction with those of JET.

AUG showed that an outward shift of n_e^{pos} can lead to an outward shift of pedestal electron pressure position (p_e^{pos}), which in turn can degrade the PB stability and hence the pedestal pressure height (p^{ped}) [8]. The change in n_e^{pos} was related to a change in gas fuelling and/or nitrogen seeding rates. In AUG, both gas fuelling and nitrogen seeding can affect the region with high density located in the high field side (high field side high density, HFSHD) [12,13] that fuels the plasma and that can modify the density position. More recently, TCV has also shown that p_e^{pos} can affect the PB stability and hence the pedestal height [11].

Instead, the role of p_e^{pos} in the ITER-like wall JET (JET-ILW) has been, so far, elusive. To date, the only detailed study [9] is in an apparent contradiction with those presented in AUG and TCV. The pedestal degradation in a JET-ILW gas scan at constant β was empirically correlated with the outward shift of n_e^{pos} but no variation in p_e^{pos} was observed. Moreover, the PB model was not able to explain the experimental results and the PB stability showed no dependence on n_e^{pos} [9]. On the other hand, the degradation of the experimental normalized

pressure gradient was clearly correlated with the increase of another parameter, the relative shift (the distance between pedestal density and temperature, defined as n_e^{pos}-T_e^{pos}).

To achieve a reliable prediction of the ITER pedestal, it is vital to reach a consistent experimental picture in all machines, with a coherent description able to clarify the roles of the pedestal position and of the relative shift in the pedestal performance.

From a theoretical point of view, the first investigation of the role of p_e^{pos} in the pedestal stability was done within the PB framework in [14], where it was shown that an inward shift of p_e^{pos} can lead to a an inward shift of the j_{bs} peak which can have a stabilizing effect on the PB modes. The PB model is the most accepted for the description of the pedestal behavior [15,16]. According to the model, the pedestal pressure increases till the PB modes become unstable and trigger the ELM. Indeed, most of the machines [17, 18, 19], including AUG [20], TCV [11], JET-C [21,22] and some JET-ILW discharges [23, 24], have shown that the pedestal pressure reaches the PB stability boundary just before the ELM crash. When the pedestal is PB limited, the experimental pedestal pressure height is in good agreement with the expectations from the PB theory. To predict the pedestal pressure height within the PB framework, the most common approach is to use the EPED model [25]. The most recent version of the EPED model [26] is based on two MHD limits. First, it is assumed that the pedestal pressure gradient (∇p^{ped}) grows unconstrained till the kinetic ballooning mode (KBM) instability is reached, after which the KBM driven turbulent transport sets the value of ∇p. Experimental measurements in DIII-D, Alcator C-mod and NSTX indeed suggests the presence of KBMs in the pedestal [27, 28, 29]. At this stage, the model assumes that the pedestal height increases via a widening of the pedestal pressure width (w_p) until the PB boundary is reached and the ELM is triggered [30, 31, 32, 33, 34, 35, 36]. According to the model, the width is supposed to increase as $w_p=D(\beta_\theta^{ped})^{1/2}$, where β_θ^{ped} is the poloidal β at the pedestal top and D is a constant that depends on the KBM boundary [26]. This expression is often called the "KBM constraint". Clear deviations from the trend $w_p \approx (\beta_\theta^{ped})^{1/2}$ have been observed so far only in NSTX [37]. The most common version of the EPED model (EPED1 [25]) assumes D=0.076, as determined from an experimental fit of DIII-D low ν^* plasmas. In literature, the experimental value of D has been observed to vary from D=0.084 in Alcator C-mod [38] to D≈0.1 in AUG [39] and JT-60U [40, 41] and in a wide range D=0.06-0.13 in JET-ILW [42] and TCV [11]. When the pedestal is PB limited, EPED can correctly predict the pedestal height in a wide range of experimental conditions and in several devices [26]. Recent results from TCV [11] have shown that more accurate predictions can be achieved if the model uses the empirically estimated D.

However, JET-ILW has shown that ELMs can be triggered even when the pedestal has not reached the PB boundary [10, 23, 42, 43]. For these types of plasmas, hereafter called for simplicity "non-PB limited", the EPED predictions can significantly overestimate the experimental pedestal height [10, 23]. It is not yet fully clear under which experimental conditions the pedestal is non-PB limited. Most of the experimental results suggest that this occurs with high gas fueling rate (Γ_D), however, the high fueling rate is not a sufficient condition, as shown in [23]. To date, it is not clear which mechanism triggers the ELMs and which mechanism sets ∇p^{ped} in the non-PB limited plasmas. Recent theoretical studies [44, 45] suggest that, in these types of plasmas, the turbulent transport driven by micro tearing modes (MTMs) might play an important role in setting ∇p^{ped}, however a firm and conclusive experimental evidence is missing. For achieving reliable pedestal predictions, it is essential to understand the physics mechanisms that set pressure gradient and width in the non-PB limited plasmas.

This work has five main goals. (I) To reconcile the JET-ILW results on the pedestal position with those of AUG and TCV, by analysing PB limited datasets. (II) To prove that the impact of p_e^{pos} on the PB stability is a general phenomenon common to all the three machines when the pedestal is PB limited. (III) To estimate the impact of p_e^{pos} on ITER performance. (IV) To understand why the previous JET-ILW results were not consistent with those of AUG and TCV. (V) To show that, when the pedestal is non-PB limited, n_e^{pos} and the relative shift might still have an impact on ∇p^{ped} by increasing the turbulent transport.

The paper is organized as follows. Section 2 describes the experimental analysis techniques and the modelling tools. Section 3 describes the datasets used. Section 4 is devoted to goals (I) and (II) and describes the pedestal behaviour of PB limited plasmas in AUG, JET-ILW and TCV. Section 5 addresses goal (III) by discussing the possible implications for the ITER pedestal and ITER fusion power. Section 6 is devoted to goals (IV) and (V) and presents the results on the link between pedestal position, micro turbulence and pedestal performance in non-PB limited JET-ILW plasmas. Finally, discussions and conclusions are presented in Section 7.

2. DATA ANALYSIS TECHNIQUE AND MODELLING TOOLS

This Section describes briefly the main diagnostics used in the work, the experimental technique for data analysis, including the definition of the key parameters and the tools used for the numerical modelling.

2.1 Diagnostics and data analysis technique.

The profiles of electron temperature (T_e) and density (n_e) are measured with Thomson scattering systems in the JET and TCV datasets. In the AUG datasets, also lithium-beam, and ECE have been used. Only the pre-ELM profiles have been considered, typically the measurements that fall in the time intervals from 70% to 99% of each ELM cycle [46]. The pre-ELM profiles are then fitted using a modified hyperbolic tangent (*mtanh*) function [47] to determine pedestal height, width and position. An example is shown in Section 4, figure 2.

The pedestal height of the total pressure (p^{ped}) in the JET datasets has been determined assuming $T_e^{ped}=T_i^{ped}$ and estimating n_i from n_e and Z_{eff} (considering Be as main impurity). The assumptions $T_e^{ped}=T_i^{ped}$ is well motivated due to the relatively high collisionality in the pedestal region [21]. A similar approach has been used in TCV, but considering C as main impurity. The total pressure in AUG has been determined using the experimental T_e and T_i and estimating n_i from n_e and the impurity density.

Due to possible uncertainty in the absolute position of the Thomson scattering diagnostics, the profiles have been shifted in order to have a specific temperature at the separatrix (T_e^{sep}). T_e^{sep} has been estimated in the three machines using a two-point model for the power balance at the separatrix [48]. In JET and AUG, the model predicts $T_e^{sep} \approx 100eV$ [49, 50] while in TCV $T_e^{sep} \approx 50eV$ [11]. Being n_e measured mainly with the same TS diagnostic, the shift applied to the density is the same as that applied to the temperature. Note that T_e^{sep} can affect the PB stability, as shown in references [42, 49]. This will be discussed in Section 7, where it is shown that a reasonable uncertainty in T_e^{sep} does not have any major effect on the conclusions of this work.

The width of the pedestal for electron temperature and density (w_{Te} and w_{ne}) are determined from *mtanh* fits to the pre-ELM profiles. For consistency with earlier results and for agreement with the EPED definition, the width of the electron pressure (w_{pe}) has been determined as $w_{pe}=(w_{Te}+w_{ne})/2$. The position of the pedestal is determined as the position of the maximum gradient of the *mtanh* fits. Widths and positions are expressed in normalized poloidal flux (ψ_N) units.

2.2 PB modelling tools.

This subsection briefly describes the method for the PB stability analysis in JET and the implementations of the EPED-like models used for the JET, AUG and TCV plasmas. For the description of the PB stability analysis techniques in AUG and TCV, we refer the reader to the relevant literature [11, 20] and references therein (no AUG and TCV PB stability diagrams are shown in this work).

PB stability for the JET plasmas.

The pedestal stability of the JET plasmas has been studied using ELITE [15] to obtain the j-α stability diagram and the self-consistent path in the j-α space.

Here j is the current density composed by fully diffused Ohmic current and bootstrap current (j_{bs}). The j_{bs} term has been calculated using the Sauter model [51]. The difference between the Sauter model and the Hager model [52] or the drift kinetic code NEO [53, 54] has been studied in [23, 52]. The three approaches agree very well at low collisionality, while the Sauter model tends to overestimate the j_{bs} in high collisionality plasmas. In terms of the stability boundary, the different j_{bs} models affect mainly the peeling boundary [23]. JET pedestal is near the ballooning boundary, so no major quantitative effect can be expected. Indeed, a quantitative comparison has shown that the different j_{bs} models lead to a negligible difference in the predicted critical normalized pressure gradient [9].

The parameter α represents the normalized pedestal pressure gradient and is defined as in [55]:

$$\alpha = -\frac{2\partial_\psi V}{(2\pi)^2} \left(\frac{V}{2\pi^2 R}\right)^{1/2} \mu_0 p' \tag{1}$$

where V is the plasma volume enclosed by the flux surface, R the major radius and p' the total pressure derivative in the poloidal flux ψ. The equilibrium has been calculated using the HELENA code [56] which takes in input the fit to the experimental T_e and n_e profiles.

A standard approach has been used to determine the stability boundary [57]. The normalized pressure gradient and the current density have been perturbed from the experimental values in order to scan the j-α space. Then, the growth rate of the most unstable mode has been determined for each j-α value. The stability criterion has been defined as $\gamma < 0.03\omega_A$ (where γ is the growth rate and ω_A is the Alfven frequency). In the stability calculation the modes from $n=5$ up to $n=70$ have been considered. The impact of different stability criteria and the use of different mode numbers have been tested in reference [23]. It has been tested that the use of higher mode numbers does not affect the stability boundary of the present datasets.

Rotation and diamagnetic effect have not been considered and they might impact the results, [19, 58, 59, 60, 61, 62, 63]. This possibility is discussed in Section 7.

The distance of the pre-ELM pedestal from the PB boundary has been quantified with the ratio $\alpha_{crit}/\alpha_{exp}$. Here, α_{exp} is the experimental normalized pressure gradient and α_{crit} is the normalized pressure gradient expected by the PB model. α_{crit} has been determined as the intersection of the self-consistent path in the $j\text{-}\alpha$ space with the PB boundary. The self-consistent path is determined by increasing the height of the pedestal temperature and then self-consistently calculating the current profile in order to find the marginally stable pedestal temperature height [49]. Examples are shown in figure 1 and discussed in Section 3. In this work, it is assumed that the pre-ELM pedestal is on the PB boundary when $\alpha_{crit}/\alpha_{exp}\approx1$, within 20%. Pedestals with $\alpha_{crit}/\alpha_{exp}>1.2$ (with α_{crit} calculated with the assumptions described above) will be dubbed as "non-PB limited".

Pedestal predictions using EPED-like models in AUG, JET and TCV plasmas.

The EPED1 model [25] is the most common tool to predict the pedestal height using the PB physics. The model uses as input parameters the experimental n_e^{ped}, β_N, plasma shape (R, a, κ, δ), Z_{eff}, plasma current and toroidal magnetic field. The model assumes that the pressure pedestal width scales as $w_p=D(\beta_\theta^{ped})^{1/2}$ with D=0.076 and that $n_e^{pos}=T_e^{pos}$. T_e^{pos} is inherently determined within EPED1 by using a specific value of T_e^{sep} and by the relation $w_p=D(\beta_\theta^{ped})^{1/2}$. The core profiles are determined by changing the core peaking in order to match the input β_N. The height of the pedestal pressure is predicted by determining the T_e^{ped} that gives the marginally PB stable profile.

In this work, two extensions of the EPED1 model have been used, iPED for AUG and TCV [20] and Europed for JET [64]. The PB stability calculations are done with MISHKA [65] in iPED and with ELITE in Europed. MISHKA and ELITE have been benchmarked on a AUG plasma, producing consistent results, with similar stability boundaries and similar position of the operational point.

The main differences with respect to the standard EPED1 is that both iPED and Europed allow to specify in input n_e^{pos} and D. So they are optimal tools to study the impact of the pedestal position on the pedestal height. Furthermore, it is possible to use Europed also with a self-consistent core-pedestal interaction. This capability releases the constraint on β_N, (which is not used anymore as an input parameter) and implements a simple core transport model. The core transport model is briefly described in section 5 when this feature is applied.

TABLE 1. *List of the eight experimental datasets used in this work. Scans 1-5 and scan 7 are fuelling rate scans at constant power in deuterium plasmas. Scan 6 is a nitrogen seeding scan at constant fuelling rate and power. Scan 8 is a gas scan at constant β_N. P is total external power, P= P_{NBI}+ P_{ECRH}+ P_{ICRH}.*

dataset	machine	description	P (MW)	gas rate (e/s)	Ip (MA)	B(T)	δ	β_N	H_{98}	PB-limited	reference
scan1	JET-ILW	Γ_D scan const. P	5	$(0.3-2)10^{22}$	1.4	1.7	0.2	1.1-1.3	0.8-0.9	yes	[23]
scan2	JET-ILW	Γ_D scan const. P	11	$(1-2.5)10^{22}$	2.0	2.2	0.4	1.2-1.4	0.7-0.9	yes	-
scan3	AUG	Γ_D scan const. P	15	$(0.5-2)10^{22}$	1.0	2.5	0.25	2.1-2.4	0.9-1.0	yes	[20]
scan4	AUG	Γ_D scan const. P	10	$(0.5-2)10^{22}$	1.0	2.5	0.25	1.6-1.9	0.8-1.0	yes	[20]
scan5	TCV	Γ_D scan const. P	1	$(0.05-2)10^{21}$	0.17	1.4	0.5	1.6-1.8	0.9-1.3	yes	[11]
scan6	TCV	Γ_N scan const. P	1	$(0-4)10^{21}$	0.17	1.4	0.5	1.5-1.8	0.9-1.2	yes	[11]
scan7	JET-ILW	Γ_D scan const. P	15	$(0.3-2)10^{22}$	1.4	1.7	0.2	1.4-2.0	0.8-1.1	no	[23]
scan8	JET-ILW	Γ_D scan const. β	7-12	$(1-8)10^{22}$	2.0	2.0	0.2	1.4	0.7-0.9	no	[9]

3. EXPERIMENTAL DATASETS.

The experimental datasets used in the work are from AUG, JET-ILW, and TCV. The datasets are summarized in table 1. Most of them are described in detail in references [9, 11, 20, 23]. These datasets have been selected due to their large variation in the pedestal position.

All datasets consist of NBI heated deuterium plasmas. The AUG datasets have an additional 1MW of ECRH. All plasmas are Type I ELMy H-modes, as determined via the increase of the ELM frequency in specific NBI power scans.

Most of the datasets are deuterium fueling rate scans at constant power. Exceptions are scan 6 and scan 8. Scan 6 is a nitrogen seeding scan performed in TCV with constant fueling rate and constant NBI power. Scan 8 is a gas scan at constant β_N in JET-ILW.

Scans 1, 3, 4, 7, 8 have been performed in low triangularity plasmas, while scans 2, 5, 6 in high triangularity. As discussed in reference [9], the
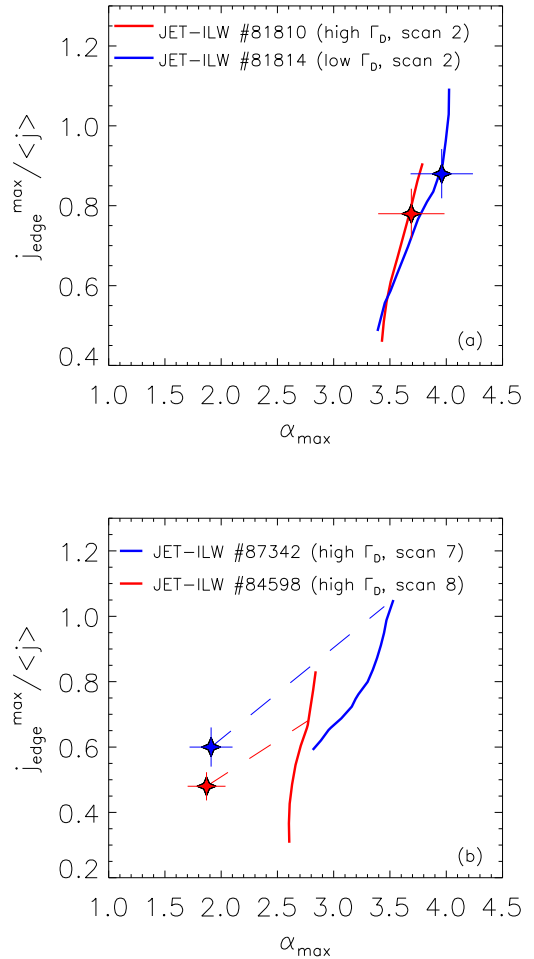

Fig. 1. *Examples of j-α PB stability diagram for (a) PB limited plasmas and (b) non PB limited plasmas. The continuous line show the PB boundary and the stars the operational point. In frame (b), the dashed lines show the self-consistent paths. Its intersection with the boundary defines the value of α_{crit}.*

triangularity does not affect the behavior of the pedestal position in gas scans.

The plasmas of the first six datasets are PB limited, as described in references [11,20,23]. As an example, the PB stability analysis for scan 2 (gas scan at high triangularity in 2MA JET-ILW plasmas) is shown in figure 1(a). In both pulses, the operational point, corresponding to the pre-ELM α_{crit} and j_{crit}, is on the PB boundary. The first six datasets are used in Section 4.

The plasmas of the last two datasets are non-PB limited at medium and high gas fueling rate [9, 23]. They are discussed in Section 6. As an example of the non-PB limited plasmas, figure 1(b) shows the PB stability analysis for the high gas pulses of scan 7 and scan 8. The operational point is significantly far from the PB boundary, in the stable region. For a quantitative comparison, the critical α has been estimated from the intersection of the self-consistent path in the $j-\alpha$ diagram with the stability boundary. In these two examples, $\alpha_{crit}/\alpha_{exp} \approx 1.9$ and $\alpha_{crit}/\alpha_{exp} \approx 1.6$. So, the normalized pressure gradient expected by the PB model is approximately 90% and 60% higher than the experimental normalized pressure gradient.

4. ROLE OF THE PEDESTAL POSITION IN PEELING-BALLOONING LIMITED PLASMAS.

The AUG and TCV results discussed in [8,11] show that the degradation of the pedestal performance with increasing fueling rate (Γ_D) is due to the reduced PB stability produced by the outward shift of the pedestal pressure. Instead, the JET-ILW results presented in [9] show that the decrease in pedestal performance with increasing Γ_D is correlated with the increase of the relative shift, while no change in p_e^{pos} is observed. These observations are indeed contradictory. However there is a major difference in these three datasets. The AUG and TCV datasets were PB limited, while the JET-ILW dataset was not PB limited at
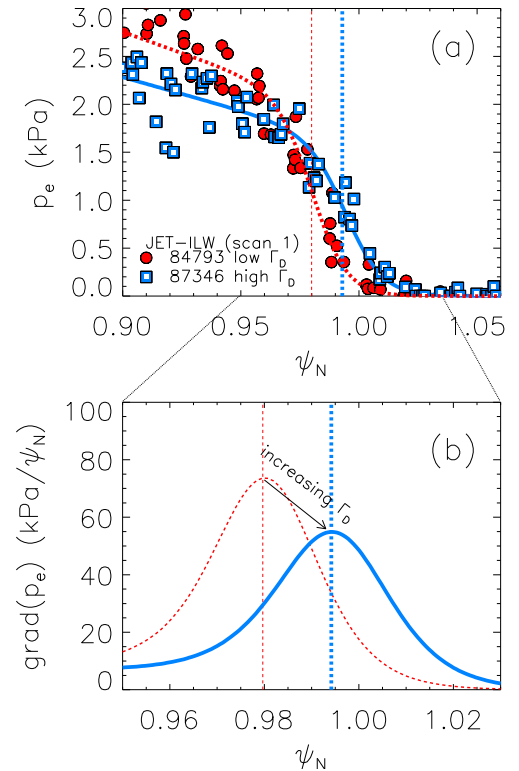

Fig. 2. (a) p_e profile for the low and the high fuelling plasmas of JET-ILW scan 1. (b) corresponding ∇p_e from the mtanh fit. The vertical dashed lines highlight p_e^{pos}.

medium and high fueling rate.

To have a consistent description of the pedestal behavior among different machines, this section is focused only on the datasets that are PB limited. The datasets used in this section are the following. For JET-ILW, a gas scan at low power and low triangularity [23] and a gas scan at medium power and high triangularity (scans 1 and 2 in table 1). For AUG, a gas scan at high and medium power with low triangularity [20] (scans 3 and 4). For TCV, a gas scan and a N seeding scan at constant power and high triangularity [11] (scans 5 and 6).

4.1 EXPERIMENTAL PEDESTAL STRUCTURE.

An example of the behavior of the p_e profile in a PB limited JET-ILW gas scan is shown in figure 2. The Γ_D increase leads to a reduction of p_e^{ped}, a reduction of the pedestal width and an outward shift of p_e^{pos}. This behavior is similar in all the PB limited fueling scans of Table 1, regardless of the machine, as shown in figure 3.

Figure 3(a) shows the pedestal height of T_e and n_e. The increasing Γ_D leads to a weak increase of n_e^{ped} and significant reduction of T_e^{ped}. As a consequence, the increase of the fueling rate leads to the reduction of p_e^{ped}. An exception from this behavior is the N seeding scan in TCV (scan 6) which produces the decrease of both T_e, n_e and p_e. This behavior is discussed in details in Section 4.3.

Figure 3(b) shows the behavior of the the electron pressure pedestal width w_{pe}. In all datasets, the increase of the gas rate leads to the
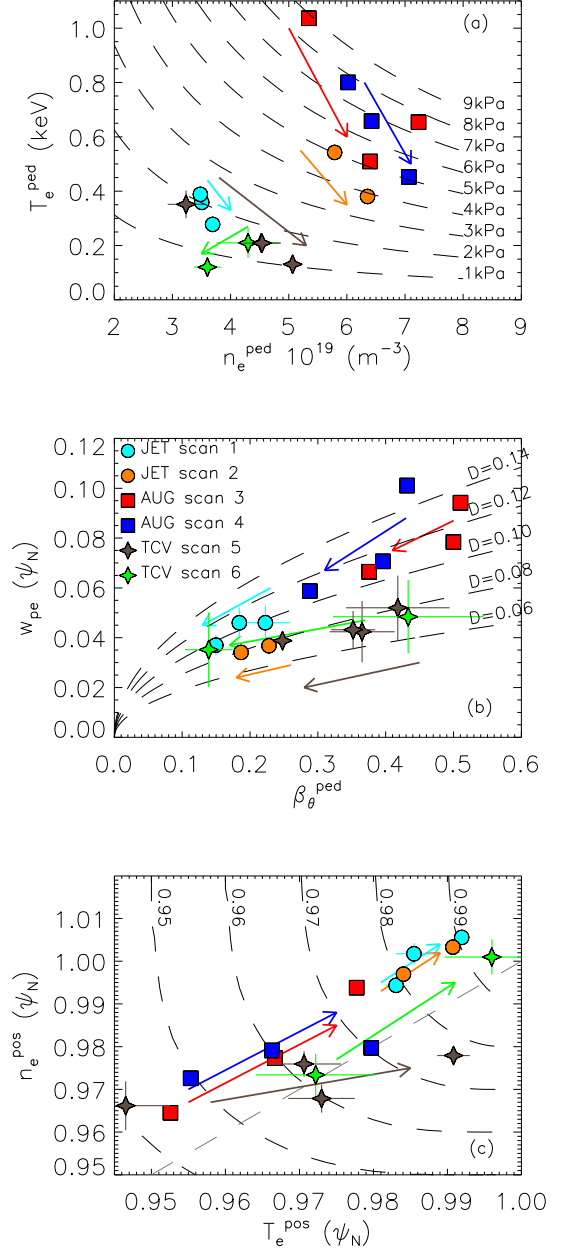

Fig. 3. (a) T_e^{ped} vs n_e^{ped}. The dashed lines show the isobars. (b) Pressure pedestal width versus β_θ^{ped}. The dashed lines show the trends $w_p=D(\beta_\theta^{ped})^{1/2}$. (c) n_e^{pos} vs T_e^{pos}. The level curves show the qualitative behavior of the corresponding p_e^{pos}. In all three frames, arrows highlight the direction of increasing gas rate. The gray-straight dashed line in frame (c) highlights the points with $n_e^{pos}=T_e^{pos}$.

reduction of β_θ^{ped} and w_{pe}. It is interesting to observe that the JET-ILW and the TCV datasets are relatively consistent with the EPED1 assumption, $w_p = D(\beta_\theta^{ped})^{1/2}$, with D in the range 0.08-0.10, while the AUG dataset is only slightly higher, with D≈0.11-0.13.

Figure 3(c) shows the pedestal position for T_e and n_e. The dashed lines represent levels curves at constant p_e^{pos} that have been geometrically determined from artificial scans of T_e^{pos} and n_e^{pos}. They can be used as a qualitative estimate of the p_e^{pos} behavior. In all cases, the increasing gas rate leads to an outward shift of n_e^{pos} and T_e^{pos} (note that, being T_e^{sep} fixed, the T_e outward shift is due to the decrase of the pedestal width). As a direct consequence of the increase of n_e^{pos} and T_e^{pos}, the pedestal pressure position moves outward as well. Another important point of discussion is the behavior of the relative shift (n_e^{pos}-T_e^{pos}). First of all, the relative shift is not zero in most of these discharges because $n_e^{pos} \neq T_e^{pos}$ (the dashed gray line highlights the points with $n_e^{pos} = T_e^{pos}$). However, especially in the AUG and JET-ILW datasets, the relative shift is roughly constant (n_e^{pos}-$T_e^{pos} \approx 1.0$-$1.5\% \psi_N$). This is because the change in n_e^{pos} is compensated by a comparable change in T_e^{pos}. As described in Section 6, the behavior of the relative shift is significantly different in the non-PB limited plasmas.
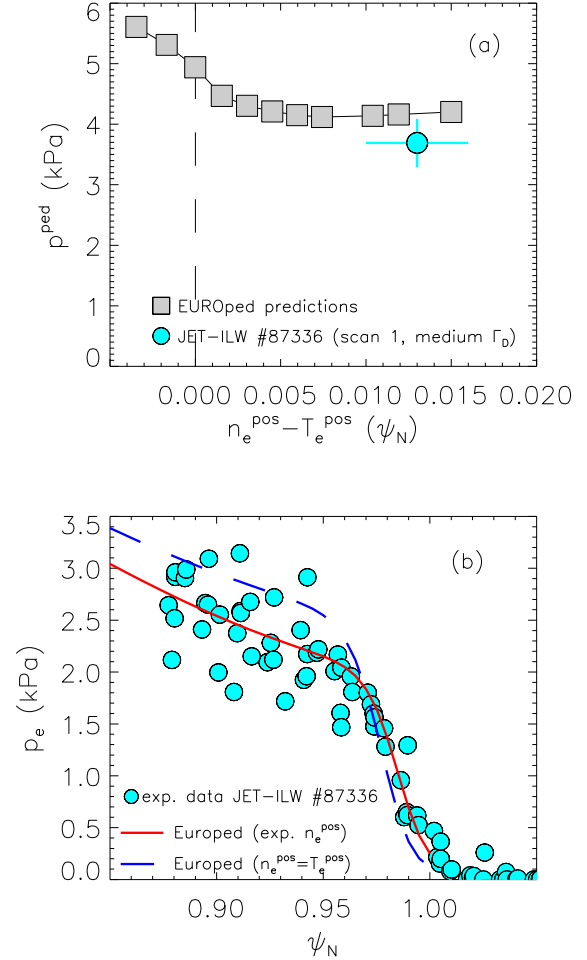

Fig. 4. (a) Predicted total pressure height using Europed versus the shift of the density position (grey squares). The blue dot shows the experimental data. The vertical dashed line highlight the standard EPED1 assumption, $n_e^{pos} = T_e^{pos}$. (b) Experimental electron pressure profile (blue dots) and corresponding critical profiles from Europed. The blue dashed line shows the critical profile obtained with the standard EPED1 assumption, $n_e^{pos} = T_e^{pos}$, while continuous red line shows the critical profile using the experimental n_e^{pos} as input.

4.2 COMPARISON WITH EPED-like MODELS.

To confirm that the pedestal degradation with increasing gas rate is linked to the p_e^{pos} outward shift, the pedestal pressure has been predicted using iPED for AUG and TCV datasets and Europed for JET-ILW datasets.

Figure 4 shows the results for a JET-ILW plasma from scan 1. The simulations have been performed without the self-consistent core-pedestal interaction, i.e. using the total beta as input parameter. In frame (a), the vertical axis represents the total pedestal pressure and the horizontal axis the density position relative to the temperature, n_e^{pos}-T_e^{pos}. The use of this horizontal axis has the advantage of showing the direct comparison with the standard EPED1 model that assumes n_e^{pos}-T_e^{pos}=0. The grey data represent the predicted pedestal height determined using different values of n_e^{pos}. As described in Section 2.2, T_e^{pos} is self-consistently determined within the code. The model predicts a clear reduction of the pedestal pressure with increasing shift. The assumption n_e^{pos}-T_e^{pos}=0 leads to a 30-35% over prediction of p^{ped}. On the other hand, a reasonable agreement is obtained when the model uses a density shift comparable to the experimental one. The outward shift of the density has led to a reduction of the PB stability and hence of the pedestal height. Note that the change in the PB stability is not a direct effect of the shift in n_e^{pos} but an indirect effect. The outwards shift of n_e^{pos} moves outwards p_e^{pos} and the j_{bs} peak and increases the separatrix j_{bs} (see Section 5.2). These are the three effects that lead to the reduction of the PB stability [8, 14].

The corresponding experimental and predicted pressure profiles are shown in Figure 4(b). The assumption n_e^{pos}=T_e^{pos} leads not only to an overestimated pedestal height, but also to a wider pedestal width. On the contrary, the Europed simulation with the experimental density position leads to a critical profile that matches extremely well both pedestal height and width.

To consolidate this result in JET-ILW, figure 5(a) shows the pedestal height of the experimental total pressure versus the fueling rate for scan 1. For comparison, the pedestal heights predicted using the two different assumptions on n_e^{pos} are shown as well. Initially, the model has been used assuming n_e^{pos}=T_e^{pos} (empty squares). The predicted negative trend with increasing fueling rate is qualitatively similar to the experimental one. This trend is due to the reduction of β_N (that is used as input parameter). It is well known that the decrease of β_N has a destabilizing effect on the ballooning modes [15, 16]. Instead, from a quantitative point of view, the assumption n_e^{pos}=T_e^{pos} overestimates the experimental pedestal pressure by $\approx$30%. As shown in figure 3(c), in these three pulses n_e^{pos} is more outward than T_e^{pos}. Using the experimental n_e^{pos} as input, the predictive Europed results are in reasonable quantitative agreement with the experimental p^{ped}, as shown by the full grey squares in figure 5(a). The difference in the predicted p^{ped} assuming n_e^{pos}=T_e^{pos} and using the experimental n_e^{pos} is $\approx$25%.

Figure 5(b) shows the predicted p^{ped} versus the experimental p^{ped} for four datasets from the three machines. The empty symbols represent the predictions with the assumption n_e^{pos}=T_e^{pos}.

The overestimation is ≈25-50% for most of the cases and almost 100% for the TCV discharge with N seeding. The full symbols represent the predictions using the experimental n_e^{pos}. The agreement with the experimental data is significantly better.

The common mechanism that emerges from the results of the PB limited plasmas in the three machines is the following. The increasing fueling rate leads to the outward shift of the pedestal density, figure 3(c). This produces the outward shift of the pressure that reduces the PB stability which, in turn, decreases the pedestal height (figure 3(a) and figure 4). Therefore, β_θ^{ped} decreases and, via the KBM constraint, the pedestal width shrinks, figure 3(b). Assuming that T_e^{sep} does not vary significantly, the shrinking of the pedestal causes the outward shift of the temperature, figure 3(c), moving the pressure further outwards and reinforcing the degradation of the pedestal height.

Fig. 5. (a) Pedestal pressure versus fuelling rate of scan 1 for experimental data (dots) and Europed prediction (squares). (b) Europed and iPED predictions versus experimental pressure for four datasets.

4.3 NITROGEN SEEDING in TCV.

As mentioned in Section 4.1, the increase of the N seeding rate in TCV has led to the p^{ped} reduction, figures 3(a). This behavior is opposite to what was observed in JET-ILW [66] and in AUG [8] where the N seeding led to an increase in p^{ped}. The reason of the increase of the pedestal performance with N in JET-ILW is still under investigation [63].

Interestingly, the (opposite) behaviors of the pedestal height with N seeding in TCV and AUG are both consistent with the PB model. The key point is that the outward (inward) shift of n_e^{pos} leads to a degradation (improvement) of the pedestal stability, no matter what the origin of the n_e^{pos} shift is. Recent seeding experiments in Alcator C-mod have shown roughly a similar behavior [67].

In TCV, the N seeding leads to the outward shift of the density which, in turns, produces the outward shift of the pressure, see figure 3(c). This has the effect of reducing the PB stability,
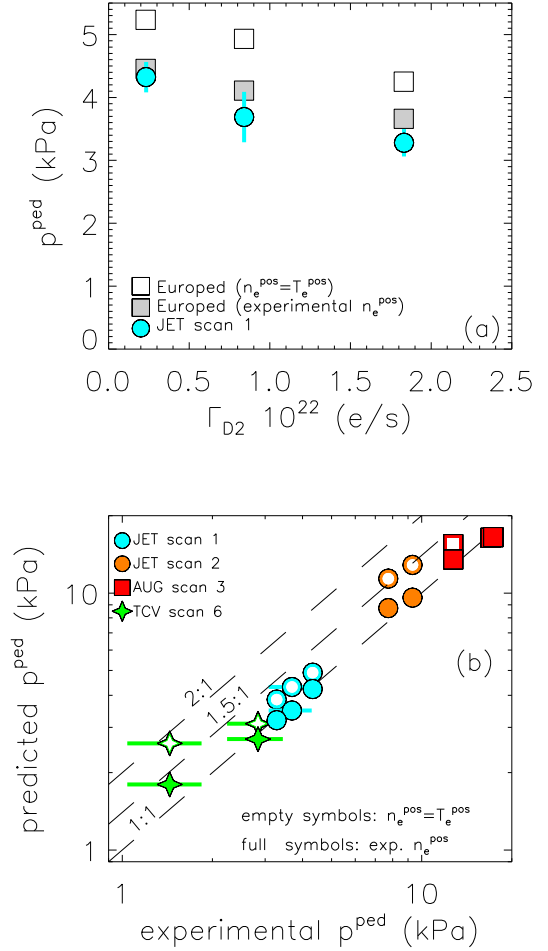
as described in Section 4.2, and hence of decreasing the pedestal height. Indeed, once the outward shift of density position is considered, iPED predicts reasonably well the pedestal height in TCV [11]. Figure 6 describes this behavior more in detail. The figure shows the pedestal height versus the corresponding n_e^{pos} for two TCV plasmas. The two pulses have identical engineering parameters apart the N seeding rate. The N seeded pulse has (i) n_e^{pos} more outward than the non-seeded by $\approx 3\% \psi_N$, (ii) pedestal height $\approx 50\%$ lower and (iii) β_N approximately 15% lower ($\beta_N \approx 1.5$ versus $\beta_N \approx 1.8$). Then, the pedestal height has been predicted using iPED for both shots using different values of n_e^{pos}. As expected, the pedestal height decreases with increasing n_e^{pos}. A 3% increase in n_e^{pos} leads to a 25-30% reduction in the predicted p^{ped}, qualitatively similar but quantitatively lower than the 50% experimental reduction. The difference is likely due to the fact that the iPED modelling is done using constant β_N and the destabilizing effect of the reduced β_N is not taken into consideration self-consistently. Nonetheless, the predicted trend are rather similar to the experimental behavior.

In AUG, the behavior is opposite but the mechanism is the same. The N seeding leads to an inward shift of the density, which leads to the inward shift of the pressure which in turn improves the PB stability and increases the pedestal height [8].

It is not clear yet why the N seeding has an opposite effect on the pedestal position in TCV and AUG. The reason might be correlated to the presence/absence of the high field side high density (HFSHD) [8,12,13]. In AUG, the N seeding reduces the HFSHD, decreasing the pedestal fueling and hence moving the density inward [8,13]. In TCV, due to the open divertor geometry, the HFSHD is likely not present, so the N seeding might simply increase the SOL fueling leading to the outward shift of the density. However, the understanding of the physics mechanism that regulates the position of the pedestal is beyond the scope of the present work.
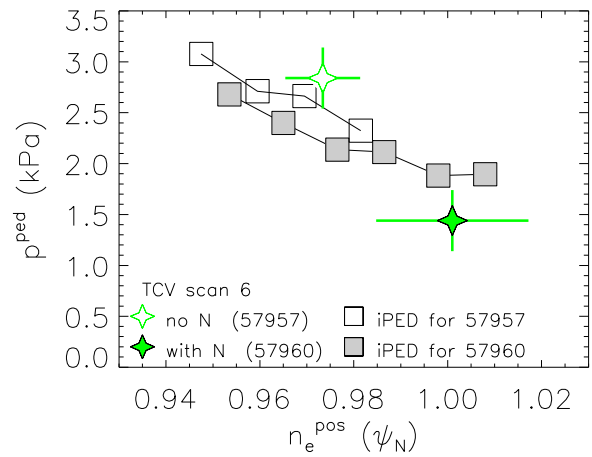
Fig. 6. Pedestal pressure versus n_e^{pos} for scan 6 of TCV. The stars shows the experimental data, while the squares the p^{ped} prediction for different values of n_e^{pos}.

In conclusion, Section 4 has shown that, when the pedestal is PB limited, the outward shift of n_e^{pos} has similar effects on AUG, JET-ILW and TCV and that EPED-like models can

reasonably predict the pedestal height, once the experimental density position is considered. Section 6 will clarify why the previous JET-ILW results were not in agreement with this behavior.

5. IMPLICATIONS FOR ITER

ITER is likely to operate at high separatrix density (n_e^{sep}) with $n_e^{sep}/n^{Greenwald} > 0.6$ [68]. Separatrix density and n_e^{pos} are strongly correlated since an outward shift of the density leads to an increase of n_e^{sep}. See later, in figure 9(a), for a qualitative example of the correlation between n_e^{sep} and n_e^{pos}.

This section estimates the impact of the density position, and hence of n_e^{sep}, on a standard ITER scenario. This is done using the ELITE code for the PB stability analysis and the Europed code for the prediction of the ITER pedestal height.

The modelling has been done on a ITER baseline scenario, with I_p=15MA, B_t=5.3T, δ=0.41, κ=1.82, assuming β_N=2.0 and $n_e^{ped}=8\cdot10^{19}m^{-3}$. Figure 7(a) shows the corresponding PB stability boundary. Initially, the PB boundary has been calculated assuming $n_e^{pos}=T_e^{pos}$ (red line) and then assuming the density is shifted outwards by $0.018\psi_N$ (blue). The change in the density position leads to the shrinking of the ballooning boundary (while the peeling boundary shows only a minimal effect). As described in Section 4, this is because the change in n_e^{pos} affects p_e^{pos} and the position of the j_{BS} peak. The operational points are shown in figure 7(a) with stars. The effect of the density shift is the reduction of the normalized pressure gradient by $\approx$15%, from $\alpha_{exp}\approx6.7$ to $\alpha_{exp}\approx5.8$.

A 15% reduction in the normalized pressure gradient suggests that the impact on ITER pedestal height might be significant. This has been tested using Europed. Initially, only the pedestal physics has been considered, i.e. without coupling self-consistently core and pedestal and assuming constant β_N. Figure 7(b) shows the predicted pressure height (estimated at ψ_N=0.93, near the pedestal top) for different values of the density shift. For each density shift, the corresponding value of n_e^{sep}/n_e^{ped} is shown on the top x-axis. The decrease in the predicted pressure with increasing shift is rather rapid, but then saturates for density shifts higher than $0.02\psi_N$. The maximum reduction of pedestal pressure is $\approx$10%. The origin of the saturation is due to the fact that, when the density shift is too large, the effect on the pressure position and on the j_{BS} is minimal, as discussed in details in the next Section.

To estimate the effect of the density shift on the ITER fusion power, P_{fus}, Europed has then been used considering self-consistently the interaction core-pedestal. The goal of the

simulation is not to give accurate values for the fusion power, but just to show qualitatively the possible effect of the density shift.

For this type of simulation, β_N is not used anymore as an external input but a simple core transport model is used. The core transport model assumes (1) low heat diffusivity (χ_e=0.1m^2/s) below a critical normalized temperature gradient length (R/L$_{Te,crit}$) and (2) a high heat diffusivity, χ_e=0.1m^2/s+2m^2/s×(R/L$_{Te}$-R/L$_{Te,crit}$), above. 70MW have been assumed as auxiliary heating located in the core. The heating by fusion α's is taken into account self-consistently [64].

The core transport model is simple, but it is sufficient to produce a rough estimate of the effect of the density position on core pressure and P$_{fus}$. The results are shown in figure 7(c) using different assumptions for the value of the critical R/L$_{Te}$. P$_{fus}$ has been estimated assuming no shift (n$_e^{pos}$=T$_e^{pos}$, red line) and assuming an outward density shift by 0.018ψ_N (blue line). The value of the critical R/L$_{Te}$ influences significantly P$_{fus}$, but the absolute reduction of P$_{fus}$ due to the density shift is rather constant ≈100MW. In relative terms, the impact of the density shift on P$_{fus}$ is from a ≈40% reduction with low R/L$_{Te,crit}$ to a ≈10% reduction with high R/L$_{Te,crit}$.
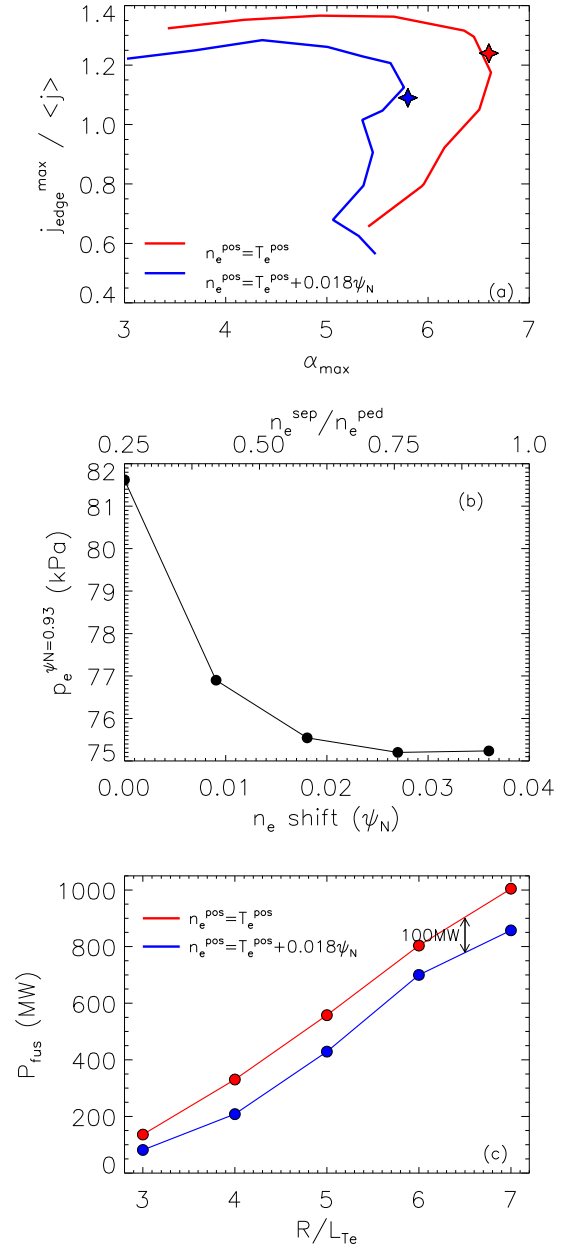

Fig. 7. (a) PB stability diagram for a ITER baseline scenario. (b) Dependence of predicted ITER pedestal pressure on the density shift. (c) Predicted P$_{fus}$ for different R/L$_{Te,crit}$. Red and blue lines in frames (a) and (c) represents respectively the assumptions $n_e^{pos}=T_e^{pos}$ and $n_e^{pos}=T_e^{pos}+0.018\psi_N$.

As a final remark, it is important to note that these conclusions are likely correlated with collisionality and triangularity. A lower collisionality (higher j_{bs}) and perhaps higher triangularity might move the ITER operational point closer to the peeling boundary. On this boundary, the effect of the density shift is less strong, figure 7(a), and its impact on the pedestal pressure and fusion power might be mitigated.

6. ROLE OF THE PEDESTAL POSITION IN PLASMAS NOT PEELING-BALLOONING LIMITED.

Non-PB limited pedestals in Type-I ELMy H-mode plasmas have been clearly identified only in JET-ILW, so far [10, 23, 42, 43]. In these types of plasmas, the EPED model significantly overestimates the pedestal pressure [23].

It is not yet clear which physics mechanism triggers the ELMs in the non-PB limited plasmas and under which operational conditions these non-PB limited pedestals appear. The main experimental evidence is that the pre-ELM pedestal of baseline discharges tends to be far from the PB boundary (in the stable region of j-α diagram) at "medium"-"high" gas fueling rate with "medium"-"high" power [9, 23, 43]. "High" gas fueling shots at low power are instead on the PB boundary [23]. Note that the meaning of "medium" and "high" is arbitrary and can be interpreted only qualitatively within gas scans and power scans. No universal threshold has been identified so far. The identification of a clear threshold in engineering and/or plasma parameters is complicated by the fact that good divertor neutral pressure measurements are not always available and by the difficulty in estimating wall sources and recycling.

The goals of this section are (i) to explain why the previous JET-ILW results [9] were not consistent with those of AUG and TCV in terms of pedestal position and (ii) to show that the low pressure gradient experimentally measured in non-PB limited plasmas might be due to an increased turbulent transport driven by the increased relative shift.

This section investigates the JET-ILW discharges in scans 7 and 8. Scan 7 is a gas scan at 15MW. Scan 8 is a gas scan at constant β_N. In both cases, the pedestal at medium and high Γ_D is non-PB limited, see figure 1(b) for the high Γ_D cases.

6.1 PEDESTAL BEHAVIOR IN THE NON-PB LIMITED DATASETS.

The JET-ILW results presented in [9] shows that the increase in the fueling rate leads to the increase in the relative shift (n_e^{pos}-T_e^{pos}). This has been experimentally correlated with the reduction of α_{exp} and hence of the pedestal performance. Figure 8(a) shows the correlation of α_{exp} versus the relative shift for scans 7 and 8. In both datasets, α_{exp} decreases with increasing relative shift. The empty circles highlight the non-PB limited pedestals and the arrow highlights the increasing fueling rate.

Figure 8(a) also shows the Europed predicted normalized pressure gradient (α_{crit}), grey squares. As expected, α_{crit} overestimates α_{exp} in the non-PB limited plasmas. Note that the model has been used with (i) the assumption $n_e^{pos}=T_e^{pos}$ (empty squares) and then with (ii) the experimental n_e^{pos} (full squares). Interestingly, the two types of assumptions do not affect the result (the full squares cover the empty squares). This is in contrast with Section 4, where a $0.01\psi_N$ density shift led to a 25% reduction in the predicted pedestal height. To understand the origin of this contradiction, it is necessary to investigate in detail the behavior of the pedestal structure.

Figure 8(b) shows the pedestal pressure width. In both datasets, a widening of the pedestal with increasing gas rate is observed, despite β_θ^{ped} decreasing or remaining constant. The behavior of the width is not as expected in the EPED1 model, where a w_{pe} reduction with decreasing β_θ^{ped} is predicted. Note that the widening of the pedestal with increasing gas rate is actually a fairly common behavior in JET-ILW, as
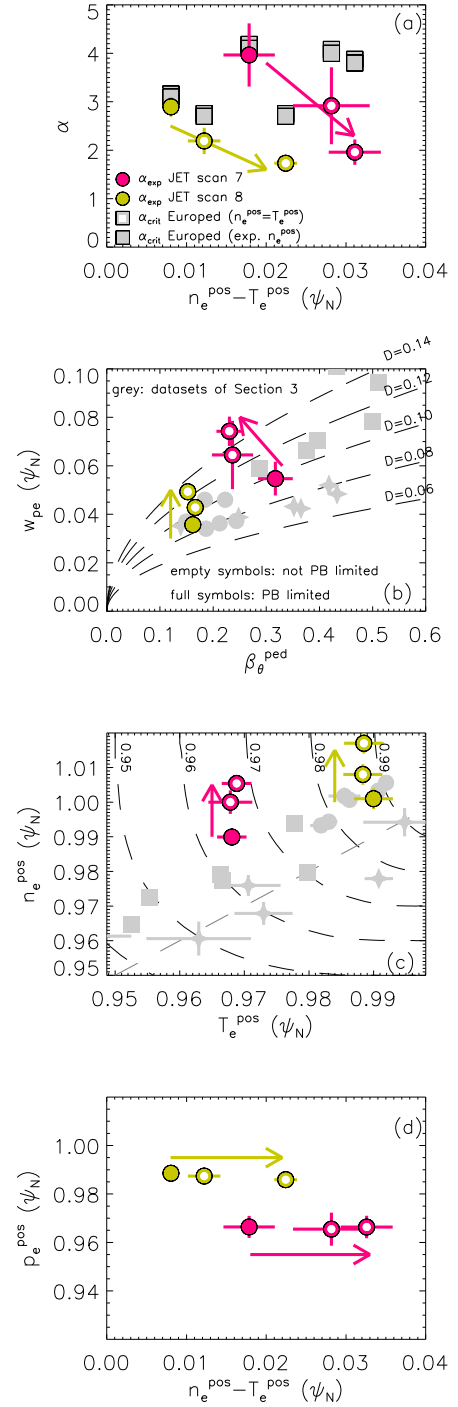

Fig. 8. (a) normalized pressure gradient vs relative shift. The dots represent the experimental data and the square the Europed predictions. (b) Pressure width vs β_θ^{ped}. Dashed lines show the trends $w_p=D(\beta_\theta^{ped})^{1/2}$. The grey data show PB limited plasmas of Section 3, for comparison. (c) n_e^{pos} vs T_e^{pos}. The level curves highlight the corresponding p_e^{pos}. The gray straight line highlights the points with $n_e^{pos}=T_e^{pos}$. The grey data show PB limited plasmas of Section 3. (d) p_e^{pos} vs relative shift. The arrows highlight the increasing gas rate. The full symbols highlight the PB limited data (low gas). The empty symbols highlight the non-PB limited data (medium and high gas).

reported in references [23, 42, 69, 70]. This behavior is significantly different from what described for the PB limited gas scans discussed in Section 4, where the pedestal shrinking with increasing gas rate was observed.

Figure 8(c) shows the behavior of the pedestal position of density and temperature. In both scans, T_e^{pos} is roughly constant, while n_e^{pos} moves outwards with increasing gas rate. This implies an increase in the relative shift. Again, the behavior is different from what was observed in PB limited datasets of Section 4, where T_e^{pos} was observed to shift outwards with increasing gas rate while the relative shift was roughly constant. The key result of figure 8(c) is that the pedestal positions of scans 7 and 8 move approximately along the level curves of constant p_e^{pos}, suggesting that the position of the pedestal pressure does not change significantly. This is verified in figure 8(d), where p_e^{pos} versus the relative shift is shown. p_e^{pos} is constant despite both the increasing relative shift and the increasing n_e^{pos}. A similar behavior is observed for the position of the j_{bs} peak, as qualitatively described in Section 6.2.

This last result explains why the Europed predictions of figure 8(a) do not show any difference using (i) the assumption $n_e^{pos}=T_e^{pos}$ and using (ii) the experimental n_e^{pos}. The PB stability is in fact affected by the pressure position and not directly by the density position. Moreover, the stability analysis considers the profiles only till $\psi_N=1.0$, so any further change outside the LCFS is not expected to influence the PB stability.

6.2 GEOMETRICAL INTERPRETATION.

A geometrical approach is useful to understand why the increasing n_e^{pos} does not affect p_e^{pos} in the non-PB limited datasets while it leads to an increase in p_e^{pos} in the PB limited datasets.

The thick lines in figure 9(a) show the T_e and n_e profiles of shot 84600 (JET-ILW low gas, PB limited pedestal of scan 8, with $n_e^{pos}-T_e^{pos}\approx0.01\psi_N$, see the full yellow dot in figure 8). From the product of T_e and n_e profile it is possible to calculate the p_e profile and the corresponding pedestal position. Then, starting from this reference case, this procedure has been repeated by shifting outwards and inwards the density profile, as shown by the colored profiles in figure 9(a). The corresponding p_e^{pos} as function of the relative shift is shown in figure 9(b). The position of the pedestal increases with increasing relative shift till $n_e^{pos}-T_e^{pos}\approx0.015\psi_N$ and then it levels off. This is because, when the relative shift is high, n_e is flat inside the separatrix and the highest density gradient is located in the region where the temperature is very low. This occurs approximately when the relative shift is larger than half the density width, as shown on the top horizontal axis in figure 9(b). With such an outward density position, the structure of the pressure gradient is dominated by the temperature,

leading to $p_e^{pos} \approx T_e^{pos}$ and to no dependence of p_e^{pos} on n_e^{pos}. This description does not consider any possible changes in the pedestal widths, but nonetheless it is sufficient to capture the main mechanism that leads to the different behavior of p_e^{pos} in the PB limited and non-PB limited datasets.

The j_{bs} has a similar behavior has shown in figures 9(c) and 9(d). The position of the j_{bs} peak increases with increasing relative shift, while the peak value of j_{bs} decreases. Saturations in both the value of the j_{bs} peak and its position are observed for $n_e^{pos}-T_e^{pos} \gtrsim 0.01\psi_N$. In figure 9, the bootstrap current has been calculated using the Sauter formula. We have verified that j_{bs} estimated with NEO [54] shows a similar qualitative behavior.

The vertical dashed lines in the right panels of figures 9 show the range of variation of the relative shift in the PB limited datasets (blue) and in the non-PB limited datasets (red). In the PB limited case, a change in $n_e^{pos}-T_e^{pos}$ leads to a change in p_e^{pos} and j_{bs}^{pos}. In the non-PB limited case, $n_e^{pos}-T_e^{pos}$ is large, in a region where p_e^{pos} and j_{bs}^{pos} have already leveled off and where the magnitude of the bootstrap peak has a slow decrease.
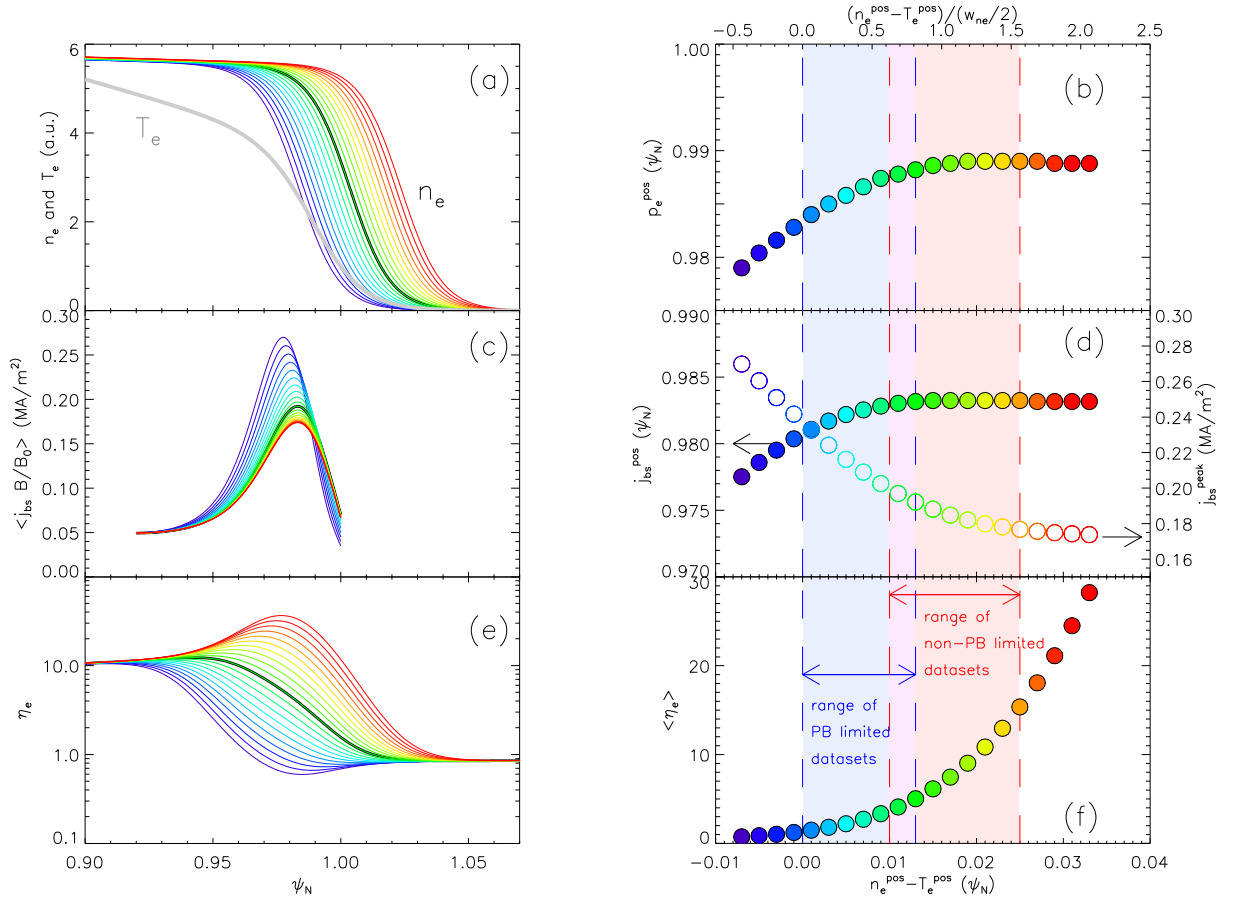

FIG. 9. (a) The thick lines shows T_e and n_e profiles for JET-ILW discharge 84600. The colored profiles show shifted n_e profiles. (b) corresponding p_e^{pos}, versus the relative shift. (c) j_{bs} and (d) position of the j_{bs} (full symbols) and maximum j_{bs} (empty symbols). (e) η_e profiles corresponding to the profiles of frame (a). (f) η_e (averaged in a region $0.02\psi_N$ wide around the position of the T_e pedestal top) versus the relative shift.

On the other hand, when the relative shift is large, n_e^{pos} has a significant impact on η_e. This parameter, defined as $\eta_e = L_{ne}/L_{Te}$ (with L_{ne} and L_{Te} the gradient length of n_e and T_e, respectively) has a significant impact on the growth rate of microinstabilities. The η_e profiles corresponding to the profiles of figure 9(a) are shown in figure 9(e). The maximum variation of η_e is almost two orders of magnitudes. To better quantify this variation, we have taken η_e averaged in a region $0.02\psi_N$ wide around the position of the T_e pedestal top (where the larger variation occurs). The correlation between $<\eta_e>$ and the relative shift is shown in figure 9(f). In the region of the PB limited datasets ($n_e^{pos} - T_e^{pos} < 0.012\ \psi_N$) the variation is minimal, while in the region of the non-PB limited datasets ($n_e^{pos} - T_e^{pos} > 0.01\ \psi_N$) $<\eta_e>$ increases significantly.

6.3 POSSIBLE ROLE OF THE TURBULENT TRANSPORT IN THE NON-PB LIMITED DATASETS.

It is well known that η_e variations have a strong influence on the microinstabilities [71, 72]. The large increase of η_e with increasing relative shift is therefore expected to drive increasing levels of temperature gradient driven micro turbulence, generating heat transport, inside the pedestal [44, 45].

Figure 10(a) shows the ratio $\alpha_{crit}/\alpha_{exp}$ versus $<\eta_e>$. The ratio $\alpha_{crit}/\alpha_{exp}$ is an estimate of the distance of the pre-ELM pedestal from the PB boundary. All JET-ILW PB limited datasets (full symbols) have $<\eta_e> \lesssim 3$, while the non-PB limited data have $<\eta_e> \gtrsim 3$. In particular, the gas scan at constant beta (scan 8) shows that $\alpha_{crit}/\alpha_{exp}$ increases with $<\eta_e>$, suggesting that temperature gradient driven microturbulence is increasingly important in these non PB limited plasmas.

To investigate the possible role of microinstabilities, the GS2 code has been used [73] and local linear gyrokinetic analysis at $\psi_N = 0.95$ (just inside the pedestal top, see figure 9(a)) have been performed for shots 84600 and 84598, see figure 10(a). $T_i = T_e$ has been assumed, so η_i and η_e are both equally enhanced in the high relative shift plasmas. Growth rates for the fastest growing modes are given in figure 10(b) as a function of perpendicular wavenumber k_y, for the ballooning angle $\theta_0 = 0$. The results show that both the ETG modes and the ITG modes are more unstable in the high relative shift plasma (non-PB limited) than in the low relative shift plasma (PB limited), with normalized growth rates on average 50% higher. A rough mixing length estimate of the thermal diffusivity suggests an increase of approximately

20% in the high relative shift / non-PB limited pedestal. No dominant unstable micro-tearing modes have been found at $\theta_0=0$ on the selected surfaces.

This first linear analysis strongly suggests that the micro turbulence driving heat transport increases with increasing relative shift inside the pedestal top. $\eta_{e,i}$ are also substantially enhanced in the pedestal, so the increased heat transport is expected to continue into the pedestal itself, which would explain the low pressure gradient observed in these non-PB limited pedestals. More extensive linear and non-linear gyrokinetic simulations are needed to explore the dependence on radius and on θ_0, and to compute the turbulent fluxes. Nevertheless, these results suggest that increased turbulent transport might explain the reduce pressure gradients in these non-PB limited pedestals.

FIG. 10. (a) $\alpha_{crit}/\alpha_{exp}$ versus $<\eta_e>$. Here, $<\eta_e>$ has been defined in the same way as in figure 9(f) by averaging the η_e profile in a region $0.02\psi_N$ wide around the T_e^{ped} position. (b) Microinstabilities growth rate versus the perpendicular wavenumber for PB limited and non-PB limited plasmas of JET-ILW scan 8.

7. DISCUSSION AND CONCLUSIONS.

A key point of the work has been the separation between the PB limited plasmas and the non-PB limited in JET-ILW. So far, non-PB limited plasmas have been identified only in JET-ILW [23, 42, 43]. In the datasets analyzed in this work, the normalized pressure gradient expected by the PB model is up to 90% higher than the experimental one, with $\alpha_{crit}/\alpha_{exp}\approx1.9$ as shown in figure 1(b) and figure 10(a). On a more general perspective, a significant part of the JET-ILW non-PB limited plasmas have $\alpha_{crit}/\alpha_{exp}>2$ [74, 75]. The PB stability in most of the earlier works (as well as in the present work) has been determined with the assumptions discussed in Section 2.2, namely $T_e^{sep}=100eV$, $T_i=T_e$ and without including possible effects from rotation and diamagnetic terms. It is important to discuss if, and how much, these assumptions can affect the present classification of PB limited and non-PB limited plasmas.
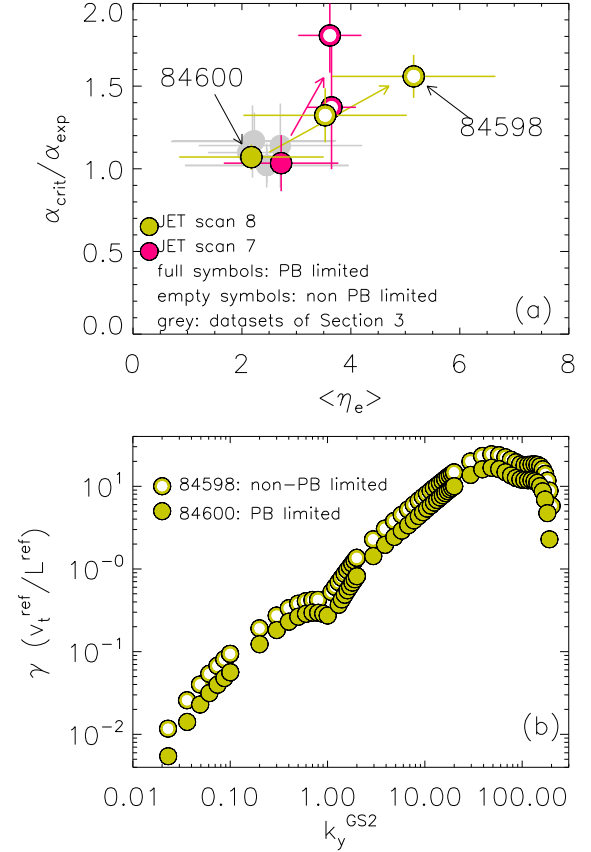
The separatrix temperature can affect the PB stability by influencing the position of the T_e pedestal and hence of the pressure [42, 57]. Indeed, it is reasonable to assume that T_e^{sep} is not perfectly constant in the scans discussed in this work. For example, in JET-ILW, the EDGE2D-EIRENE simulations discussed in [76] suggest that gas and power scans without seeding can lead to $\approx 10\%$ variation in T_e^{sep}. However, the pedestal is very steep so a reasonable change in T_e^{sep} has a minimal effect on T_e^{pos} and on the pedestal pressure. As a
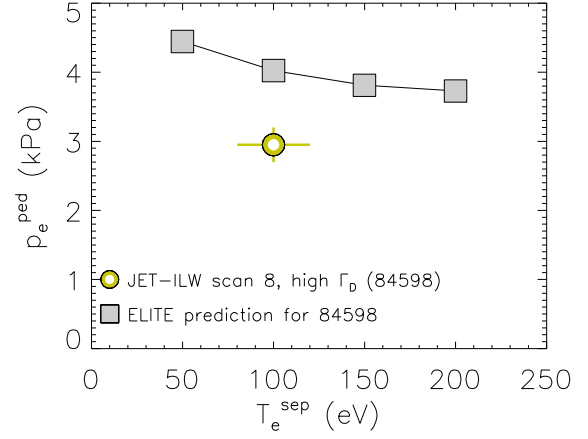

FIG. 11. Electron pedestal pressure and separatrix tempurate for the JET-ILW high fuelling plasma (non-PB limited) from scan 8. The circle shows the experimental data and the squares show the predicted p_e^{ped}.

practical example, the effect on shot 84598 (non-PB limited plasmas of scan 8 discussed Section 6) has been estimated. A 10% uncertainty in T_e^{sep} leads to only a $\approx 0.0015\psi_N$ variation in T_e^{pos}, from $\psi_N = 0.985$ at 100eV to $\psi_N = 0.9865$ at 110eV (a variation in T_e^{pos} that is lower than its experimental uncertainty). Such small variation has no significant effect on the predicted pedestal pressure. Figure 11 estimates the impact of T_e^{sep} on the predicted p_e^{ped} assuming a more extreme (likely unrealistic) variations, from $T_e^{sep}=50$eV to $T_e^{sep}=200$eV. The increase of T_e^{sep} reduces the PB stability and the predicted pedestal height, from $p_e^{ped}\approx 4.5$kPa at $T_e^{sep}=50$eV to $p_e^{ped}\approx 3.8$kPa at $T_e^{sep}=200$eV. However, the predicted pressure still remains significantly higher than the experimental pressure. Moreover, the shot used in figure 11 is at the high end of the fueling scan, so T_e^{sep} is more likely to be lower than 100eV. This would have a stabilizing effect, moving the stability boundary further away from the experimental pedestal. Therefore, we can exclude that the uncertainty on T_e^{sep} can explain why datasets 7 and 8 are not PB limited.

Unfortunately, it is very challenging to test in scans 7 and 8 if the assumptions $T_i=T_e$ and if rotation and diamagnetic term can affect the conclusions on the non-PB limited plasmas. These effects have been studied in detail in JET-ILW in references [61, 62, 63]. The inclusion of rotation can, in some cases, reduce the PB stability. The impact on the PB boundary can vary on a shot to shot basis with the maximum observed effect of $\approx 25\%$ [62, 63]. This can, in principle, significantly reduce the gap between the PB boundary and the operational point in the non-PB limited plasmas. However, at present, it is not clear if the inclusion of rotation would be sufficient to explain the value $\alpha_{crit}/\alpha_{exp}\approx 1.9$ observed in the pulses of Section 6 (or the higher values $\alpha_{crit}/\alpha_{exp}>2$ observed in other JET-ILW datasets). No conclusive claim is

possible at this stage on the plasmas analyzed in this work. A detailed investigation of the rotation effect is out of the scope of the present work and will be subject for future studies.

It should be noted that the datasets discussed in this work are composed of plasmas in Type I ELMy H-modes. Specifically, the non-PB limited plasmas discussed in Section 6 are part of wider power scans that show a clear increase of the ELM frequency with increasing P_{sep} [23]. So, it is not easy to motivate the distance of the operational point from the PB boundary with the argument that the ELMs are not Type I.

The present work has shown that the lower pedestal pressure gradient in the non-PB limited plasmas might be due to increased turbulent transport. However, the mechanism that triggers the ELMs in these types of plasmas still remains unclear. Some hypotheses for the ELM trigger have been proposed in [77]. For example, the pre-ELM pedestal might reach the KBM limit and the ideal MHD ballooning modes could start to grow exponentially driven by non-linear physics [78]. Another possibility might be related to the divertor oscillation observed in some non-PB limited plasmas [77]. If these divertor oscillations were linked to oscillations in the plasma volume or position, the ELM triggering mechanism might be similar to that in experiments with vertical kicks [79] that was modeled with the JOREK code [80].

The change in the position of the pedestal density has shown to be very important for the pedestal performance. Experimental results show that the density position moves outwards with increasing fueling rate and with increasing power in JET-ILW [9] and with increasing fueling rate and decreasing nitrogen seeding in AUG [8]. The full understanding of the physics mechanism that leads to the n_e^{pos} variation is out of the scope of the present work. Anyhow, it is important to discuss the current understanding. In AUG, the physics mechanism that regulates n_e^{pos} is understood and is related to the presence of the HFSHD [8, 12 13]. For example, the nitrogen seeding reduces the HFSHD which, in turn, reduces the SOL and the pedestal fueling and effectively leads to the inward shift of the density. In JET-ILW and TCV, instead, the mechanism is not clear yet. In TCV, the HFSHD is likely not present due to the open divertor configuration. HFSHD experimental measurements are still not available in TCV. In JET-ILW, the HFSHD has been experimentally observed [12]. However, no clear and consistent correlations with n_e^{pos} have been documented yet, as discussed in [81, 82]. In JET, the present working hypothesis is that the increase of the fueling rate leads to the increase of the SOL opacity and hence to a lower neutral penetration. EDGE2D-EIRENE modelling to test this hypothesis are currently ongoing.

In conclusion, the work has investigated the role of the pedestal position in the pedestal performance and has tried to resolve the apparent contradictions in the published results on the topic. A key point has been to distinguish between plasmas with a pedestal that is PB limited and plasma with a pedestal that is not PB limited.

In plasmas that are PB limited, the outward shift of the density leads to the outward shift of the pedestal pressure which in turn destabilizes the PB modes, reducing the pedestal height. This type of behavior, already described in AUG and TCV [8, 11] has now been consistently observed also in JET-ILW. In this type of plasmas, the PB model describes the pedestal behavior well and EPED-like predictions reproduce the experimental data correctly once the realistic density position is used.

Assuming that the ITER pedestal is PB limited, this work has estimated the impact of the shift of the pedestal density on the ITER baseline scenario. The ITER pedestal is supposed to degrade at most by 10%, while the impact on the fusion power is supposed to vary between 10% and 40% depending on the critical R/L_{Te}.

In plasmas that are not PB limited, the behavior of the pedestal structure with increasing gas rate is quite different. First of all, the pedestal widens instead of shrinking with increasing gas. Then, the density still moves outwards but no significant change has been observed in the pressure position. Therefore, the PB model cannot properly describe the pedestal behavior and EPED-like models significantly overestimates the pedestal height. The work suggests that the lower pressure gradient observed in the non-PB limited plasmas might be explained by an increase of turbulent transport driven by ETG and ITG modes.

The work on the non-PB limited plasmas is just at the beginning and several questions still remain open. Assuming that the lower pressure gradient is due to the increased turbulent transport, it is not yet clear which physical mechanisms trigger the ELMs. Moreover, it is not yet clear under which experimental conditions the plasma becomes non-PB limited. The increase of the gas rate seems a key factor, but a universal threshold has not been found yet. Finally, it is not clear why the pedestal widens with increasing gas instead of shrinking like in the PB limited case. Understanding the behavior of the pedestal width is a key factor for understanding why the pedestal position behaves differently in the PB limited and non-PB limited plasmas.

REFERENCES

[1] J.G. Cordey et al., *Plasma Phys. Control. Fusion* **38** A67 (1996)
[2] M. Beurskens et al., *Plasma Phys. Control. Fusion* **51**, 124051 (2009)
[3] M.N.A. Beurskens et al., *Phys. Plasmas* **18**, 056120 (2011)
[4] R. Maingi, Phys. Rev. Lett. **103**, 075001 (2009)
[5] R. Maingi et al., *Nucl. Fusion* **52** 083001 (2012)
[6] T.H. Osborne et al., *Nucl. Fusion* **55** 063018 (2015)
[7] J.W. Hughes et al., *Nucl. Fusion* **47** 1057 (2007)
[8] M. Dunne et al., *Plasma Phys. Control. Fusion* **59**, 014017 (2017)
[9] E. Stefanikova et al., *Nucl. Fusion* **58**, 056010 (2018)
[10] L. Frassinetti et al., *Plasma Phys. Control. Fusion* **59**, 014014 (2017)
[11] U. Sheikh et al., *Plasma Phys. Control. Fusion* **61**, 014002 (2019)
[12] Potzel S. et al., J. Nucl. Mater. **463**, 541 (2015)
[13] Reimold et al., Nucl. Mater. Energy **12**, 193 (2017)
[14] J. Lönnroth et al., Nucl. Fusion **51**, 013003 (2011)
[15] Wilson H.R. *et al.*, *Phys. Plasmas* **9** 1277 (2002)
[16] Snyder P.B. *et al.*, *Phys. Plasmas* **9** 2037 (2002)
[17] H. Urano, *Nucl. Fusion* **54**, 116001 (2011)
[18] R. Groebner *et al.,* *Nucl. Fusion* **53**, 093024 (2013)
[19] N. Aiba *et al.,* *Nucl. Fusion* **51**, 073011 (2011)
[20] M. Dunne et al., *Plasma Phys. Control. Fusion* **59**, 025010 (2017)
[21] M. Beurskens et al., *Nucl. Fusion* **53** 013001 (2013)
[22] M. Leyland et al. Nucl. Fusion **53**, 083028 (2013)
[23] C. Maggi et al., *Nucl. Fusion* **55**, 113031 (2015)
[24] C. Giroud et al., *Plasma Phys. Control. Fusion* **57** 035004 (2015)
[25] P.B. Snyder *et al.*, *Phys. Plasmas* **16** 056118 (2009)
[26] P.B. Snyder *et al.*, *Nucl. Fusion* **51** 103016 (2011)
[27] Z. Yan *et al.*, *Phys. Rev. Lett.* **107** 055004 (2011)
[28] A. Diallo *et al.*, *Phys. Plasmas* **20** 012505 (2013)
[29] A. Diallo *et al.*, *Phys. Rev. Lett.* **112** 115001 (2014)
[30] R. Groebner *et al.,* *Nucl. Fusion* **49**, 045013 (2009)
[31] R. Groebner *et al.,* *Nucl. Fusion* **50**, 064002 (2010)
[32] E. Wolfrum *et al.*, *Plasma Phys. Control. Fusion* **51** 124057 (2009)
[33] A. Burchart *et al.*, *Plasma Phys. Control. Fusion* **52** 105010 (2010)
[34] A. Diallo *et al.,* *Nucl. Fusion* **51**, 103031 (2011)
[35] D. Dickinson *et al.,* *Plasma Phys. Control. Fusion* **53** 115010 (2011)
[36] J. Hughes *et al.,* *Nucl. Fusion* **53**, 043016 (2013)
[37] A. Diallo *et al.,* *Nucl. Fusion* **53**, 093026 (2013)
[38] J.R. Walk et al. , *Nucl. Fusion* **52** 063011 (2012)
[39] P.A. Schneider et al., *PPCF* **54**, 105009 (2012)
[40] H. Urano *et al.,* *Nucl. Fusion* **48**, 045008 (2008)
[41] H. Urano *et al.,* *Nucl. Fusion* **49**, 095006 (2009)
[42] L. Frassinetti et al., *Nucl. Fusion* **57**, 061012 (2017)
[43] M. Beurskens et al., *Nucl. Fusion* **54** 043001 (2014)

[44]D.R. Hatch et al., *Nucl Fusion* 56, 104003 (2016)

[45] D.R. Hatch et al., *Nucl Fusion* 57, 036020 (2017)

[46] L. Frassinetti et al., Rev. Sci. Instrum. 83, 013506 (2012)

[47]R.J. Groebner et al., Nucl. Fusion **41**, 1789 (2001)

[48] P.C. Stangeby 2000 The Plasma Boundary of Magnetic Fusion Devices (Bristol: Institute of Physics Publishing)

[49]S. Saarelma et al., *Phys. Plasmas* **22** 056115 (2015)

[50] H.J. Sun et al. Plasma Phys. Control. Fusion **59** 105010 (2017)

[51] Sauter O. and Angioni C. *Phys. Plasmas* **6** 2834 (1999)

[52] R. Hager Phys. Plasmas **23**, 042503 (2016)

[53]Belli E. *et al.*, *Plasma Phys. Control. Fusion* **54** 015015 (2012)

[54]Belli E. *et al.*, *Plasma Phys. Control. Fusion* **56** 045006 (2014)

[55] Miller R.L. *Phys. Plasmas* **5** 973 (1998)

[56]Huysmans G.T.A. *et al, Computational Physics: Proc.Int. Conf. (Amsterdam, The Netherlands, 1991) (Singapore: World Scientific)*

[57] S. Saarelma et al., *Phys. Plasmas* **53** 123012 (2013)

[58]N. Aiba *et al., Nucl. Fusion* **50**, 045002 (2010)

[59] H. Urano *et al., Nucl. Fusion* **47**, 706 (2007)

[60] H. Urano *et al., Nucl. Fusion* **51**, 113004 (2011)

[61] N. Aiba et al., *Nucl. Fusion* **57**, 126001 (2017)

[62] N. Aiba et al., *Nucl. Fusion* **60**, 014032 (2018)

[63] C. Giroud et al., EX/3-3, 27th IAEA Int. Conf. on Fusion Energy, Gandhinagar, 2018.

[64]S. Saarelma et al., *Plasma Phys. Control. Fusion* **60**, 014042 (2018)

[65] A.B. Mikhailovskii et al., Plasma Phys. Rep. **23** 844 (1997)

[66] C. Giroud et al., *Nucl Fusion* **53**, 113025 (2013)

[67] M. Dunne et al., EX/P8-2, 27th IAEA Int. Conf. on Fusion Energy, Gandhinagar, 2018.

[68] A.S. Kukushikin, Journal of Nuclear Materials **438**, 203 (2013)

[69] M. Leyland et al. Nucl. Fusion **55**, 013019 (2015)

[70]C. Maggi et al., Nucl. Fusion **57**, 116012 (2017)

[71]D. Dickinson D et al., Phys. Rev. Lett. **108**, 135002 (2012)

[72] J. Hillesheim et at Plasma Phys. Con. Fus. **58**, 014020 (2016)

[73] M. Kotschenreuther et al.,Comput.Phys.Comm. **88**, 128 (1995)

[74] L. Frassinetti et al., 45th EPS Conf. on Plasma Physics, Prague, Czech Republic, 2-6 July 2018, P4.1027

[75] S. Saarelma et al., 60th Annual Meeting of the APS Division of Plasma Physics, Portland, Oregon, 5–9 November (2018). TI2.00002

[76] J. Simpson et al., "Using EDGE2D-EIRENE to simulate the effect of impurity seeding and fueling on the upstream electron separatrix temperature" 23rd International Conference on Plasma Surface Interactions in Controlled Fusion Devices (PSI-23) , Princeton, NJ, USA.

[77]C. Bowman et al., Nucl. Fusion **58**, 016021 (2018).

[78]H.R Wilson et al., Phys. Rev. Lett **92**, 175006 (2004)

[79] E. de la Luna et al. Nucl. Fusion **56**, 026001 (2015)

[80] F.J. Artola et al. Nucl. Fusion **58**, 096018 (2018)

[81] C. Giroud et al., EX/P6-13, 26th IAEA Int. Conf. on Fusion Energy, Kyoto, 2016.

[82] E. de la Luna et al., EX/P6-11, 26th IAEA Int. Conf. on Fusion Energy, Kyoto, 2016.